A Fully Wireless and Batteryless Localization System With 50 Micrometre Motion Detection Capability and Adaptive Transmitter Power Control for Point-of-Care Biomedical Applications

Arkaprova Ray ⓘ, *Graduate Student Member, IEEE*, Iman Habibagahi ⓘ, *Graduate Student Member, IEEE*, and Aydin Babakhani ⓘ, *Senior Member, IEEE*

Abstract—**Localization has varied applications in biomedicine, such as wireless capsule endoscopy (WCE), detection of cancerous tissue, drug delivery, robotic surgeries, and brain mapping. Currently, most localization systems are battery-powered and suffer from issues regarding battery leakage and limited battery life, resulting in potential health hazards and inconveniences when using them for continuous health monitoring applications. This article proposes an entirely wireless and battery-less 2D localization system consisting of an integrated circuit (IC) that is wirelessly powered at a distance of 4 cm by a 40.68 MHz radio frequency (RF) power of only 2 W. The proposed localization system wirelessly transmits a locked sub-harmonic 13.56 MHz signal generated from the wirelessly received 40.68 MHz RF power signal, eliminating the need for a power-hungry oscillator. Additionally, the system, having a measurement latency of 11.3 ms, has also been verified to sense motion as small as 50 μm as well as measure the rate of motion up to 10 beats per minute, therefore extending its application to the detection of physiological motions such as diaphragm motion during breathing. The localizer has a small form factor of 17 mm $\times$ 12 mm $\times$ 0.2 mm and consumes an average power of 6 μW. Ex vivo measurements using the localizer inside the porcine intestine demonstrate a localization accuracy of less than 5 mm.**

Index Terms—**Localization, wireless, battery-less, energy harvesting, motion detection, biomedical, capsule endoscope.**

I. Introduction

THE advent of the Internet of Things (IoT) in recent years has led to its increasing use in biomedical applications to enhance healthcare delivery, patient monitoring, and disease management [1], [2]. Wireless sensor networks (WSNs) play an important role in transmitting and receiving data to and from devices in IoT and can either be battery-powered or wirelessly powered. Battery-powered WSNs have limitations such as the limited lifetime, chemical leakage, and failure of batteries, therefore limiting their use in wearable or implantable biomedical applications, leading to wirelessly powered WSNs becoming increasingly popular for these applications. Localization is the process of accurately determining the position or location of an object. Localization of wireless sensor networks (WSNs) is particularly significant for biomedical applications where accurate and precise data collection is essential for monitoring the vital signs of patients to facilitate timely intervention, disease diagnosis, and treatment. Moreover, the constraints imposed by wireless powering have given rise to research focusing on using cheaper methods and more power-efficient hardware to localize these WSNs [3], [4], [5].

Among the variety of applications that require localization of WSNs, biomedical applications form an important class. One such application is wireless capsule endoscopy (WCE) for treating gastrointestinal (GI) tract diseases. Conventionally, treatment of GI tract diseases has involved surgical endoscopy, which is performed by inserting probes into the GI tract, causing great pain and inconvenience to the patient. WCE, on the other hand, requires the patient to swallow capsules, which have the capability to receive and transmit data. These capsules, therefore, provide an alternative painless procedure for monitoring the GI tract. The localization of such capsules, which form the nodes of a WSN, is therefore of paramount importance to provide information about the location of tumors and other abnormalities in the GI tract. Other biomedical applications of localization include automated drug delivery and robotic surgeries [6] in which prior knowledge of the location is crucial. Localization can also become an important feature in implantable biomedical sensors for detecting the location of epileptic electrical activity in the brain [7]. Cardiac ablation procedures [8], which involve inserting catheters into veins or arteries, could also be greatly simplified using the localization of WSNs. Therefore, localization has a broad range of biomedical applications which are extremely essential for the advancement of humanity.

Prior work on the localization of WSNs for biomedical applications has broadly focused on two significant approaches: (1) Magnetic localization and (2) Electromagnetic (EM) wave-based localization. Magnetic localization has two major

advantages. Due to similar values of permeability in air and animal tissue, there is lesser signal attenuation inside the animal body for low-frequency magnetic fields. Moreover, it does not require the node to be in the line of sight with the transmitter (TX) and the receiver (RX). Therefore, magnetic localization has a higher accuracy as compared to other methods [9], [10]. However, the absence of ferromagnetic materials must be ascertained to ensure high accuracy since they interfere with the magnetic field used for localization. Among the EM waves, radio frequency (RF) has most commonly been used. RF-based localization provides savings in hardware compared to magnetic localization using permanent magnets. Using coils to generate magnetic field gradients overcomes this limitation at the cost of a large form factor and generating a large amount of heat for a large field of view (FOV). Therefore, RF-based localization can be implemented with a smaller form factor, and lower cost [9], [10]. However, RF signals are attenuated by different amounts at different locations inside the animal body. Therefore, proper characterization of the medium is required before localization. The choice of frequency is also important for such methods. Higher frequency signals do not pass through the animal tissue. Lower frequency improves penetrability through animal tissues but reduces accuracy.

Over the years, the rapid scaling of CMOS has enabled a reduction in the IC size and, therefore, that of the nodes used. Today, the size of these nodes is almost entirely dominated by the size of passives. In RF-based localization, the requirements for penetration of RF signals through animal tissue, skin, and bones limit their frequencies to less than a few hundred megahertz (MHz). Reducing the form factor of the localization system requires the design of millimeter-scale coils or antennas. At such frequencies, the constraints on antenna size reduce the efficiency of the wireless link [11], [12]. This entails the usage of either higher TX power or the design of an IC having lower power consumption. The localization accuracy also directly depends on the Signal-to-Noise Ratio (SNR) at the receiver. A larger received signal power is therefore required to obtain an improved SNR. At MHz-range frequencies, the TX and RX antennas are almost always in the near field. Attempts to increase the operating range of the link lead to increased path loss ($\propto 1/r^6$) and, therefore, lesser received power. Therefore, multiple transmitting nodes with the same frequency and phase can be used to increase the received signal power. A conventional technique to do this is using oscillators in phase-locked loops (PLLs) [13] or injection-locked power oscillators [14], [15], [16]. PLLs require a crystal oscillator, while injection-locking suffers from limited locking range. Since both these techniques are extremely power-hungry, it is a challenge to synchronize these nodes for low-power applications efficiently.

In the past few years, numerous systems have performed localization in literature. Authors in [17] used a magnetic gradient-based change in oscillator frequency for 2D localization. This approach reduces the dependency of localization on the variance of the received RF signal power due to the intervening medium while using the magnetic field for spatial information. However, the resolution of the frequency shifting depends on the phase noise characteristics of the oscillator, necessitating the use of a
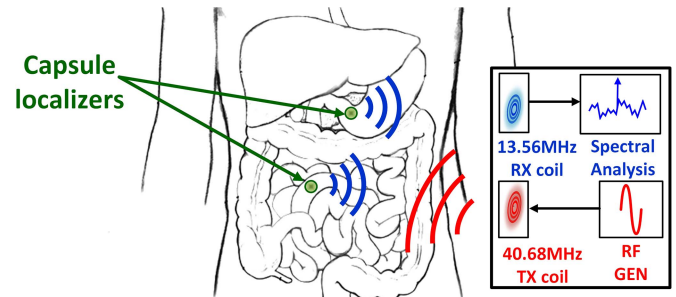

Fig. 1. Conceptual representation of proposed localization system.

PLL to reduce the phase noise before the transmission phase, subsequently increasing the power budget. Further, due to the small coil sizes, the operating range of the system is only 3 mm. Authors in [18] used magnetic beacons to generate alternating magnetic fields at low-MHz frequencies for 3D localization, which helps in reducing the TX power and coil size. Each beacon generates an excitation signal at a different offset frequency. This work also suffers from limited resolution due to oscillator phase noise. Further, the system uses many TX coils spread over a large spatial dimension, making it unsuitable for point-of-care applications. Both [17] and [18] are battery-powered, although the power consumption is low enough for wireless powering. This limitation gives rise to the need for periodic battery or capsule replacement, which is highly inconvenient. Authors in [19] implemented the 2D localization of a capsule endoscope using the compensated received signal strength indicator (RSSI) technique. However, the transceiver ICs in this work are battery-powered, resulting in a lifetime of about 12 hours. The power consumption of the transmitter inside the capsule is 1.7 mW, which makes wireless powering infeasible. Authors in [20] implemented magnetic gradient-based 3D localization for capsule endoscopy and had a maximum range of over 1 m with a penetration depth of 40 cm. Although the capsule had a longer lifetime of up to 4 weeks, it remains battery-powered. This work also requires an excitation power as high as 800 W for the non-portable system and 60 W for the portable system to generate static magnetic fields. Even though the rise in temperature is less than 0.1°C per minute for the portable version, a heat dissipation mechanism is required since it might become an important safety consideration if the capsule is inside the GI tract for a long time.

This article is an extended version of [21] and presents a detailed qualitative and quantitative analysis of the circuit design used in the IC and the wireless power transfer link. Fig. 1 shows the conceptual representation of the proposed localization system in [21] for reference. Moreover, this article also presents additional experimental results based on a technique for sensing and detecting motion as small as 50 μm using the power of the 13.56 MHz received signal. The power of the received signal has also been used to modulate the power of the RF signal generator, therefore leading to a reduction of up to 50% in the TX power. The rest of the article is organized as follows. Section II discusses the system architecture. Section III discusses the coil design procedure for an efficient wireless power transfer link design.
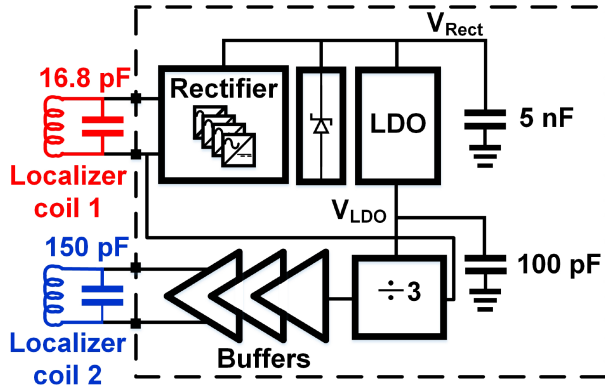
Fig. 2.   Localizer architecture.

Fig. 3.   Circuit model of the wireless power transfer (WPT) link between (a) TX coil and localizer coil 1 and (b) localizer coil 2 and RX coil.

Section IV discusses the details of circuit implementation and simulation results. Section V describes the measurement setup and results. Finally, Section VI concludes the article.

II. SYSTEM ARCHITECTURE OVERVIEW

Fig. 2 shows the architecture of a localizer. The localizer includes an integrated circuit (IC) (enclosed by dashed lines) wire bonded on a PCB and two planar coils fabricated on the same PCB. Each of these coils has a diameter of 8 mm. The IC comprises a cross-coupled rectifier, an LDO, and a digital divide-by-3 circuit. The TX coil couples a continuous-wave sinusoidal RF signal at a frequency of 40.68 MHz to localizer coil 1 connected to the input of the rectifier. The RF power is harvested by the rectifier, generating a DC voltage at the input of the LDO. The LDO generates a regulated supply voltage of 1.1 V for the divide-by-3 circuit. The divide-by-3 utilizes the 40.68 MHz TX signal and divides its frequency by 3 to generate a locked sub-harmonic 13.56 MHz signal, therefore eliminating the need for power-hungry oscillators or PLLs. The 13.56 MHz signal at the output of the buffers following the divide-by-3 is coupled to the RX coil through localizer coil 2. Using two separate frequencies for transmitting and receiving prevents interference of the received signal with the TX power signal and ensures more localization accuracy. The wireless power transfer (WPT) link is optimized to ensure reliable wireless powering of the system at a maximum distance of 40 mm with 2 W of external power.

III. WIRELESS POWER TRANSFER LINK DESIGN

Fig. 3 illustrates the circuit model for the wireless power transfer (WPT) link between (a) the TX coil and localizer coil 1 and (b) localizer coil 2 and the RX coil. Since the two links have similar characteristics, only the link shown in Fig. 3(a) is analyzed, and the insights obtained have been applied to the design of the other link. The link efficiency (η_{link}) is given by the product of the efficiency of the localizer coil (η_{loc}) and that of the TX coil (η_{TX}) [22]. The maximum η_{TX} is obtained when the operating frequency is equal to the resonant frequency (ω_{res}) of the localizer coil. Since the input resistance of the rectifier (R_{in}) is much larger than the resistance of the localizer coil (R_{loc}), a
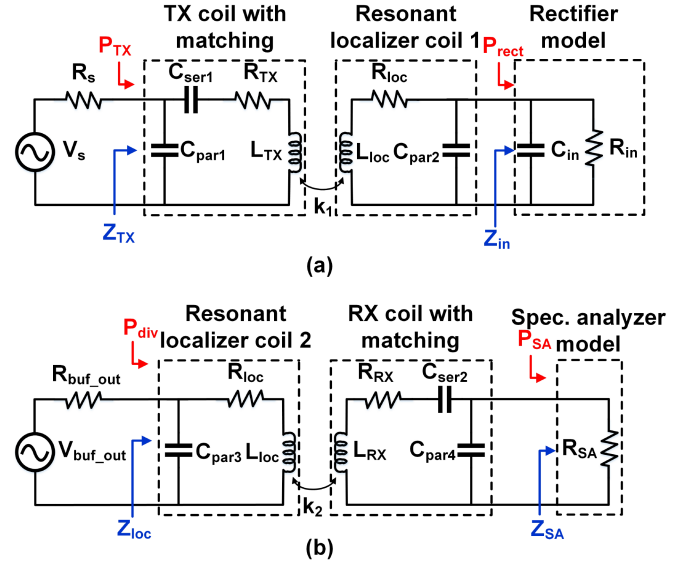
parallel capacitance C_{par2} is used to resonate the localizer coil at its operating frequency of 40.68 MHz [22]. In such a topology, ω_{res} is given by

$$\omega_{res}^2 = \frac{1}{L_{loc}(C_{par2} + C_{in})}. \tag{1}$$

where L_{loc} is the inductance of the localizer coil and C_{in} is the input capacitance of the rectifier as shown in Fig. 3(a). Similarly, C_{par3} is used to resonate localizer coil 2 at its operating frequency of 13.56 MHz. Off-chip ceramic capacitances C_{par2} and C_{par3} of values 16.8 pF and 150 pF respectively were therefore connected in parallel to the localizer coils, improving the power received and transmitted by the localizer at these desired frequencies. η_{loc}, η_{TX}, and η_{link} of the link are then given by [22]

$$\eta_{loc} = \frac{Q_{loc_L}}{Q_{rect}} \tag{2}$$

$$\eta_{TX} = \frac{k^2 Q_{TX} Q_{loc_L}}{k^2 Q_{TX} Q_{loc_L} + 1}. \tag{3}$$

$$\eta_{link} = \eta_{loc} \eta_{TX}. \tag{4}$$

where Q_{rect} is the quality factor of the load given by $Q_{rect} = R_{in}/\omega L_{loc}$, Q_{loc_L} is the loaded quality factor of the localizer coil given by $Q_{loc_L} = Q_{loc} Q_{rect}/(Q_{loc} + Q_{rect})$ ($Q_{loc} = \omega L_{loc}/R_{loc}$), Q_{TX} is the quality factor of the TX coil given by $Q_{TX} = \omega L_{TX}/R_{TX}$, and k is the distance-dependent coupling factor between the TX coil and the localizer coil. The coupling factor can be determined from the self and mutual inductances of the coils or can also be empirically given by [22]

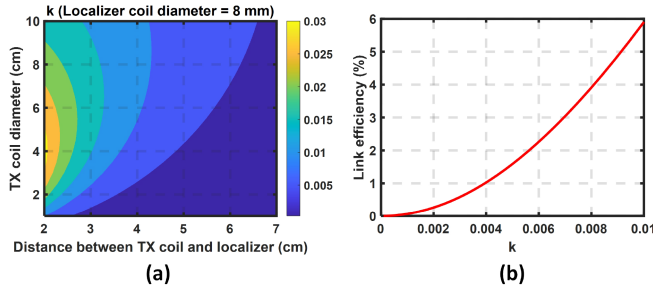$$k = \frac{d_{TX}^2 d_{loc}^2}{8\sqrt{d_{TX} d_{loc}}\left(D^2 + \frac{d_{TX}^2}{4}\right)^{\frac{3}{2}}}. \tag{5}$$

Fig. 4. (a) Coupling coefficient k between TX coil and localizer coil 1 with respect to the distance between TX coil and localizer for a localizer coil diameter of 8 mm and (b) Calculated link efficiency versus coupling coefficient.

TABLE I
DESIGN PARAMETERS OF COILS USED

	Localizer coil	TX coil	RX coil
Trace width (mm)	0.18	1.1	1.1
Trace separation (mm)	0.26	1.1	1.1
Diameter (mm)	8	35	45
Substrate	FR4	FR4	FR4
No. of layers	2	2	2
Substrate thickness (mm)	0.2	1.6	1.6
Turns per layer	6	3	6
Self-resonant frequency (SRF) (MHz)	100.74	59.08	17.95
Quality factor (Q)	63.77 at 40.68 MHz (simulated) 48.59 at 13.56 MHz (simulated)	44.03 at 40.68 MHz (measured)	26.99 at 13.56 MHz (measured)
Inductance (μH)	0.96 (simulated)	1.91 (measured)	12.5 (measured)
$|S_{11}|$ (dB)	NA	-22.73	-15.42

where d_{TX} and d_{loc} are the diameters of the TX coil and localizer coil, respectively, while D is the distance between these coils. The diameter of the localizer coils is constrained to 8 mm to minimize the form factor of the entire system, thereby enabling the use of these localizers in capsules for endoscopy. Fig. 4(a) shows the coupling factors obtained using (5) for a localizer coil diameter of 8 mm as the diameter of the TX coil and distance between the TX coil and localizer are varied. At a distance of 4 cm, a maximum coupling factor of 0.01 can be obtained for a TX coil diameter of 10 cm. The coupling factor also does not change much at larger distances when the diameter of the TX coil is increased. Therefore, a diameter of 3.5 cm is chosen for the TX coil. Fig. 4(b) plots the link efficiency calculated using (2), (3) and (4) as a function of the coupling factor at a distance of 4 cm between the TX coil and localizer. The parameters of the designed TX coil and localizer coil given in Table I have been chosen for this plot. A maximum of 6% link efficiency is obtained for a coupling factor of 0.01.

From (4), it can be deduced that the link efficiency increases with an increase in the values of k, Q_{TX} and Q_{loc}. The larger self-inductance of the TX coil and localizer coil improves the link efficiency for wireless power transfer (WPT) by increasing the quality factor of each of these coils. Since the localizer coils have extremely small inductance due to their small diameter, (1) the trace widths of these coils are minimized, (2) the number
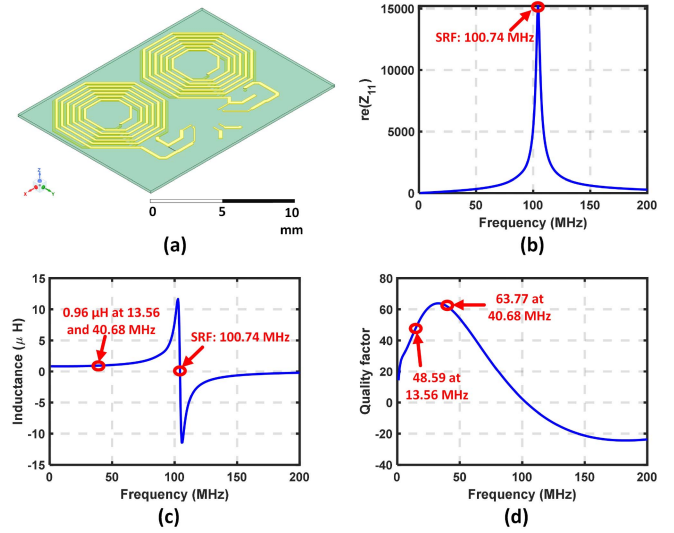

Fig. 5. (a) HFSS schematic with two localizer coils and the simulated (b) $re(Z_{11})$, (c) inductance, and (d) quality factor of each localizer coil in the absence of a resonating capacitor.

of turns is maximized, and (3) the thickness of the substrate is reduced to obtain the maximum possible value of inductance. Therefore, these coils are fabricated on a 0.2 mm thick two-layer FR4 substrate with 6 turns on each layer. Since these coils are small, the parasitic inductance of connectors is comparable to the coil inductance, making it unfeasible to measure their s-parameters or inductance using commercially available equipment such as a vector network analyzer (VNA) [23]. Fig. 5 shows (a) the Ansys HFSS schematic of the localizer and the simulated (b) real part of Z_{11}, (c) inductance, and (d) quality factor of each localizer coil when it is not connected to the resonating capacitance.

The TX and RX coils are designed to have a large quality factor and a self-resonant frequency (SRF) close to the operating frequency to improve the link efficiency. The performance of these coils is measured using a Keysight N5230 C PNA-L Network Analyzer. Fig. 6 shows the (a) TX coil and its measured (b) real part of Z_{11}, (c) inductance, and (d) quality factor while Fig. 7 shows the same parameters for the RX coil. The TX and RX coils are matched to 50 Ω for maximum power transfer. The path loss of the TX and RX links is simulated using Ansys HFSS. Fig. 8(a) shows the simulated path loss between the TX coil and the localizer coil 1 at 40.68 MHz, while Fig. 8(b) shows the simulated path loss between the localizer coil 2 and the RX coil at 13.56 MHz. Since R_{in} varies from 9 $k\Omega$ to 16 $k\Omega$ (as shown in Fig. 10(d)) over the range of input powers, the path loss between the TX coil and the localizer coil 1 at 40.68 MHz is simulated for these two values of R_{in} to obtain the possible range of path loss. Moreover, the path loss between the localizer coil 2 and the RX coil is simulated for an R_{buf_out} of 5 $k\Omega$ since it is equal to the simulated output resistance of the buffer (as shown in Fig. 14(c)). The distance between the TX coil and the localizer coil 1 is varied from 0 to 4 cm, while that between the RX coil and the localizer coil 2 is varied from 0 to 12 cm. Table I describes the details of the coil design parameters.
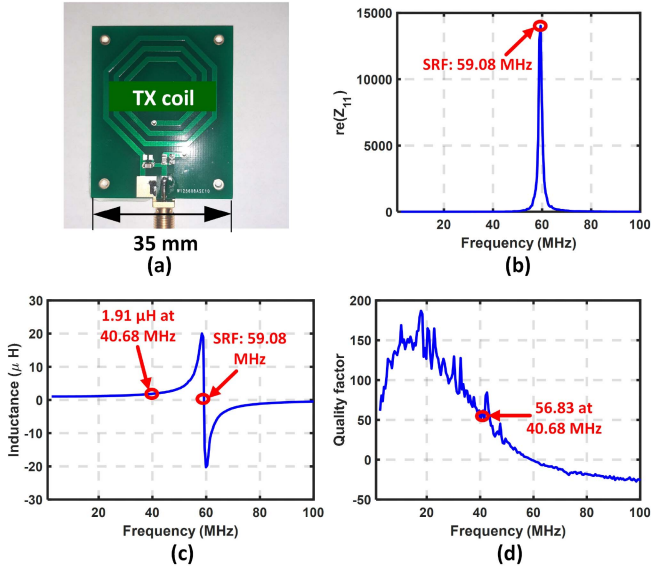
Fig. 6. (a) TX coil and its measured (b) $re(Z_{11})$, (c) inductance, and (d) quality factor when it is not matched.
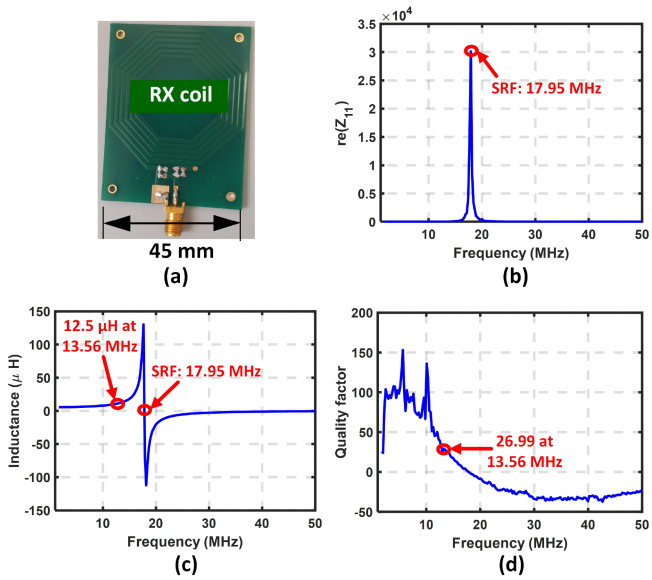

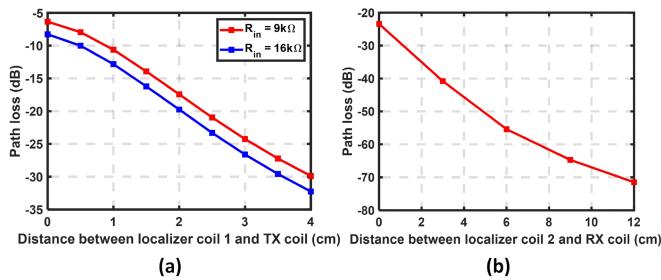Fig. 7. (a) RX coil and its measured (b) $re(Z_{11})$, (c) inductance, and (d) quality factor when it is not matched.

Fig. 8. Simulated path loss between (a) TX coil and localizer coil 1 at 40.68 MHz for $R_{in} = 9\ k\Omega$ and $R_{in} = 16\ k\Omega$ and (b) RX coil and localizer coil 2 at 13.56 MHz for $R_{buf\_out} = 5\ k\Omega$.
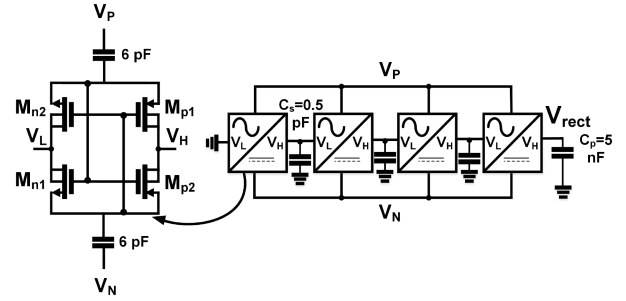

Fig. 9. Schematic of four-stage passive cross-coupled rectifier.
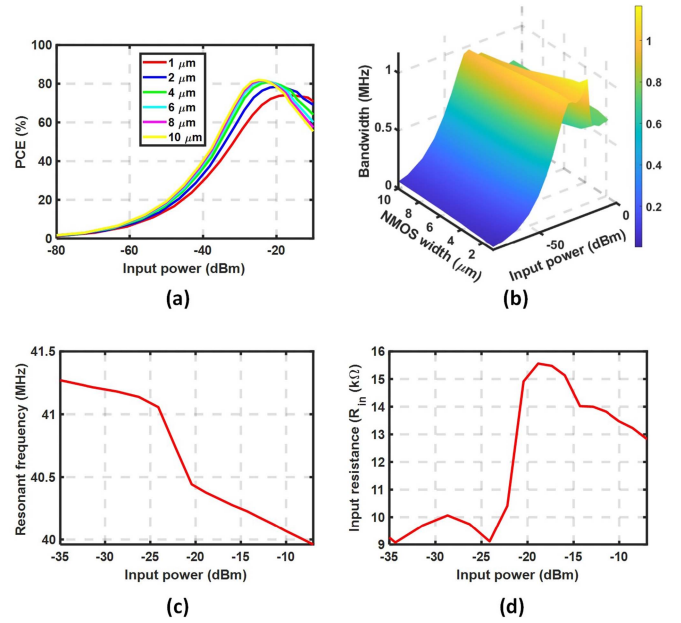

Fig. 10. Simulated (a) PCE and (b) bandwidth of the rectifier for different transistor widths and input RF powers. (c) and (d) show the variation in localizer resonant frequency (determined by the variation in C_{in}) and variation in R_{in} respectively with different input RF powers for the selected W/L = 4 μm/0.18 μm.

IV. CIRCUIT IMPLEMENTATION

A. Rectifier

A passive full-wave CMOS rectifier having four stages is used to convert the wirelessly received 40.68 MHz RF signal to a DC voltage. Each stage of the rectifier incorporates a cross-coupled topology, as shown in Fig. 9. When V_P is greater than V_N, transistors M_{p1} and M_{n1} are turned on, while transistors M_{p2} and M_{n2} are turned off. The charge on the coupling capacitor connected to V_P is therefore used to charge the output node of the rectifier stage (V_H). On the other hand, when V_N is greater than V_P, transistors M_{p2} and M_{n2} are turned on, while transistors M_{p1} and M_{n1} are turned off. In this half cycle, the charge on the coupling capacitor connected to V_N is used to charge V_H. The power conversion efficiency (PCE) of a rectifier is the ratio of the power delivered to the load at the output of the rectifier
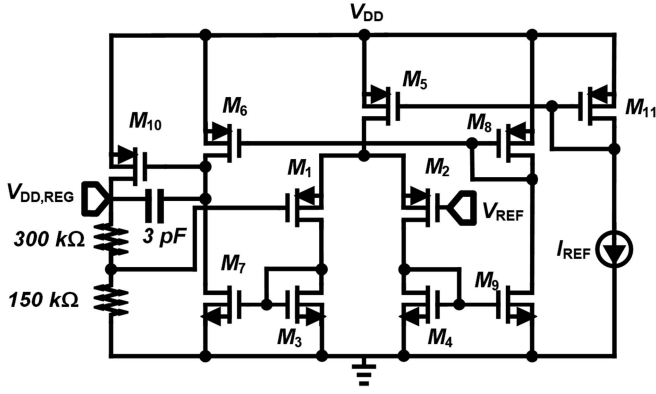
Fig. 11.   Schematic of the LDO.

P_{OUT} to the RF power supplied at its input P_{RF}. It is given by

$$PCE = \frac{P_{OUT}}{P_{RF}} = \frac{P_{OUT}}{P_{OUT} + P_{LOSS}}. \qquad (6)$$

where P_{LOSS} is the effective power loss in the rectifier. An important parameter in the design of the rectifier is its bandwidth given by

$$BW = \frac{f_0}{Q_{rect}} \qquad (7)$$

where f_0 is the operating frequency and Q_{rect} is the quality factor of the rectifier, as defined earlier. Since C_{in} of the rectifier varies with input power, ω_{res} given by (1) also changes. A higher rectifier bandwidth is, therefore, essential for reliable wireless powering of the localizer. The rectifier is simulated for an output voltage of 1.1 V using an input 40.68 MHz RF signal of power ranging from −80 dBm to 0 dBm at a constant load current of 12.75 μA, which is the maximum current that the LDO draws from the rectifier output. Fig. 10 illustrates the (a) PCE and (b) bandwidth of the rectifier for different NMOS transistor widths and input powers. Higher PCE is obtained using larger transistors, but the bandwidth drops due to increased input resistance. Therefore, the aspect ratio of NMOS transistors is chosen to be 4 μm / 0.18 μm. The PMOS transistor widths are chosen to be double that of the NMOS transistors. Fig. 10(c) shows the variation in the resonant frequency of the localizer ω_{res} due to the variation in C_{in} of the rectifier with input power, while Fig. 10(d) shows the variation in its input resistance R_{in} for the selected transistor aspect ratio. Since this variation in R_{in} only changes the path loss between the TX coil and the localizer coil 1 by 2 dB (illustrated in Fig. 8(a)), it can be concluded that the rectifier has enough bandwidth to withstand the changes in ω_{res}.

Another critical parameter is the sensitivity of the rectifier, which is defined as the minimum RF power required at its input for generating the minimum required voltage at its output for proper operation of the circuit at the desired load. Reducing the rectifier sensitivity is therefore paramount for increasing the link efficiency and, subsequently, the operating range of the wireless power transfer (WPT) system. In this work, the cross-coupled topology is chosen due to its superior sensitivity and PCE among its counterparts [21], [24], [25]. Deep n-well NMOS transistors

are used to enable the connection between source and bulk, reducing the source-bulk potential for the subsequent rectifier stages and, consequently, the threshold voltage, leading to better sensitivity and PCE. As mentioned in Section IV-B, an LDO output voltage of 1.1 V is targeted, while the LDO has a dropout voltage of 47.64 mV. Therefore, the minimum rectifier output voltage for proper operation is approximately equal to 1.16 V. The sensitivity of the rectifier simulated at an output voltage of 1.16 V and a load current of 12.75 μA is obtained to be equal to 32 μW. For each stage, coupling capacitors of 6 pF are chosen to couple the signal to the input of the rectifier with an attenuation of less than 1%. A 5 nF on-chip storage capacitor C_p is used to reduce the ripple at the output of the rectifier. A diode limiter is used to limit the rectifier output voltage V_{rect} to less than 3.8 V, therefore preventing the breakdown of transistors.

B. Low-Dropout Regulator (LDO)

The output of the rectifier acts as the line voltage of the LDO. The LDO is required to generate a regulated DC voltage of 1.1 V at its output, which is used as the supply voltage for the IC. Fig. 11 depicts the schematic of the LDO. It includes an error amplifier that compares a reference voltage (V_{REF}) of 336 mV and the voltage generated by the resistive division of the output. The reference voltage is generated using a bandgap reference generator with proportional-to-absolute-temperature (PTAT) architecture. The pass transistor of an LDO can either be a PMOS device acting as a voltage-controlled current source (VCCS) or an NMOS device acting as a source follower. LDOs with current source pass transistors have higher loop gain and lower dropout voltage as compared to those with source followers [26]. Therefore, an LDO with a current source is used in the design. The pass transistor in such a topology is typically a large device to reduce the dropout voltage [26]. The pass transistor is therefore sized appropriately to generate a low dropout voltage at the highest load current, and the feedback resistor values of 300 and 150 $k\Omega$ are chosen to minimize quiescent power consumption. The LDO requires a smoothing capacitor of 100 pF at its output, which can easily be implemented on-chip. For an LDO with an on-chip output capacitor, the worst-case stability condition occurs when the load current is zero. Therefore, based on the value of the smoothing capacitor, a 3 pF Miller compensation capacitor is chosen to ensure LDO stability under the zero-load current condition. Fig. 12(a) and (b) show the simulated magnitude and phase of the loop gain of the LDO, respectively, under two conditions: zero and 10 μA load current. It can be observed from Fig. 12 that the LDO has a low-frequency loop gain of 31.53 dB and a phase margin of 57.79 degrees at a unity-gain bandwidth of 21.14 kHz when the load current is zero. The loop gain drops to 30.3 dB, and the unity-gain bandwidth increases to 25.22 kHz when the load current is 10 μA.

Specifications of the LDO include the quiescent current consumption, which is the static current consumed by the LDO when the load current is zero. Line and load regulations are other important specifications that quantify the variation in the LDO output voltage with changes in line voltage and load current at
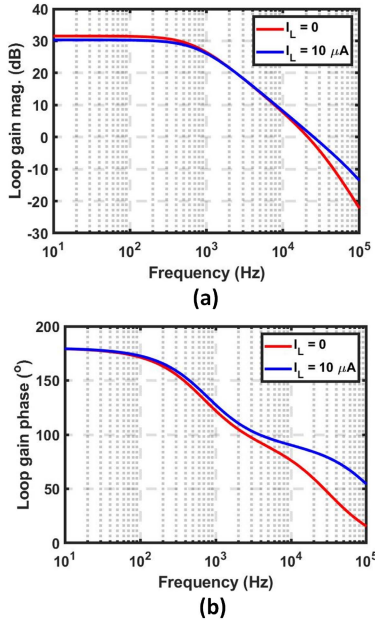
Fig. 12. Simulated loop gain (a) magnitude and (b) phase of the LDO.
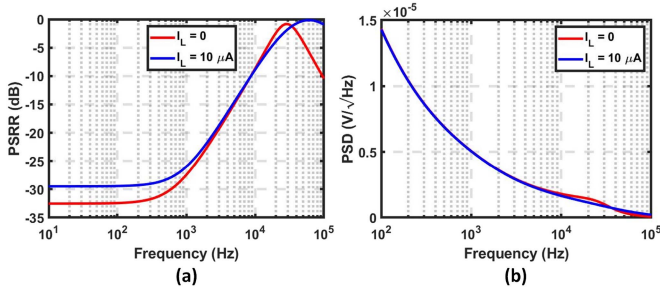

Fig. 13. Simulated (a) PSRR and (b) power spectral density of output noise for the LDO.

steady state and are defined as

$$\text{Line Regulation} = \left.\frac{\Delta V_{LDO}}{\Delta V_{Rect}}\right|_{t\to\infty} \times 100\%. \qquad (8)$$

$$\text{Load Regulation} = \left.\frac{\Delta V_{LDO}}{\Delta I_{LOAD}}\right|_{t\to\infty}. \qquad (9)$$

The load regulation of the LDO is related to its closed-loop DC output resistance. The power supply rejection ratio (PSRR) measures the amount of ripple at the output of the LDO due to a ripple at its input. Therefore, the line regulation of an LDO is equal to its PSRR at DC. Fig. 13(a) shows the simulated PSRR of the LDO, while Fig. 13(b) shows the power spectral density (PSD) of the noise at the LDO output. Table II summarizes the specifications of the LDO.

C. Divide-By-3 and Buffers

Fig. 14(a) shows the schematic of the divide-by-3 circuit. It includes a mod-3 counter and an additional D flip-flop to generate a 50% duty cycle signal at its output. The designed flip-flops are conventional master-slave flip-flops and have an

TABLE II
SUMMARY OF LDO SPECIFICATIONS

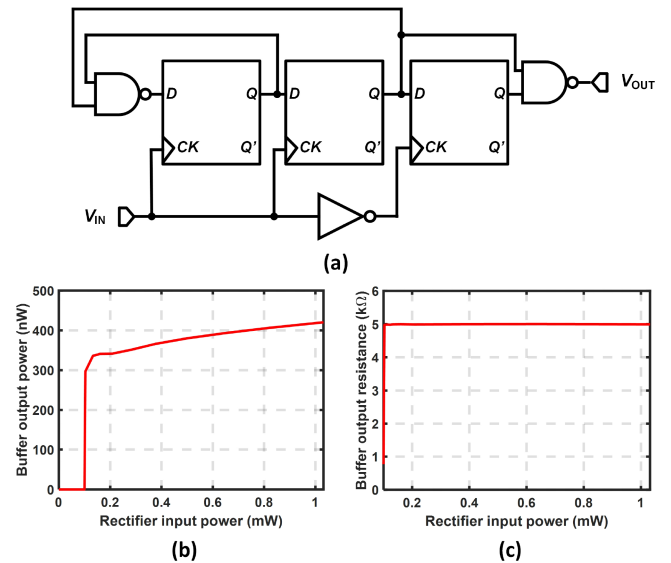| Parameter	Value
Preset output voltage (V_{LDO})	1.1 V
Load current (I_L) range	0-10 μA
Dropout voltage	47.64 mV at $I_L = 10\mu A$
Quiescent current (I_Q)	2.75 μA
Line Regulation	<0.2% for both $I_L = 0$ and $10\mu A$
Load Regulation	562Ω
PSRR ($I_L = 10\mu A$)	-29.48 dB at 10 Hz
	-26 dB at 1 kHz
	-8.9 dB at 10 kHz
PSRR ($I_L = 0$)	-32.53 dB at 10 Hz
	-27.46 dB at 1 kHz
	-8.9 dB at 10 kHz
PSD of output noise	14.31 $\mu V/\sqrt{Hz}$ at 100 Hz
	0.22 $\mu V/\sqrt{Hz}$ at 100 kHz

Fig. 14. (a) Schematic of the divide-by-3 circuit; (b) Output power of the buffer versus rectifier input power, when the buffer is loaded by the circuit parameters of the localizer coil 2 and (c) Output resistance of the buffer versus rectifier input power.

asynchronous set-reset functionality. The divide-by-3 circuit consumes 1 μW power. Fig. 14(b) depicts the power at the output of the buffer following the divide-by-3 circuit with respect to the input power of the rectifier when the buffer is loaded with the circuit parameters of localizer coil 2. The sensitivity of the localization system is determined by that of the rectifier and the divider-buffer combination. The sensitivity of the rectifier has already been defined earlier. The sensitivity of the divider-buffer combination, on the other hand, is defined as the minimum power at the input of the rectifier for which it generates a detectable 13.56 MHz signal at the output of the buffer. From Fig. 14(b), it can be observed that the sensitivity of the divider-buffer combination is 99 μW. The sensitivity of the divider-buffer combination, therefore, dominates over that of the rectifier. Fig. 14(c) shows the output resistance of the buffer with respect to the input power of the rectifier. It can be observed that once the divider-buffer combination turns on, the buffer has a constant output resistance of around 5 kΩ.
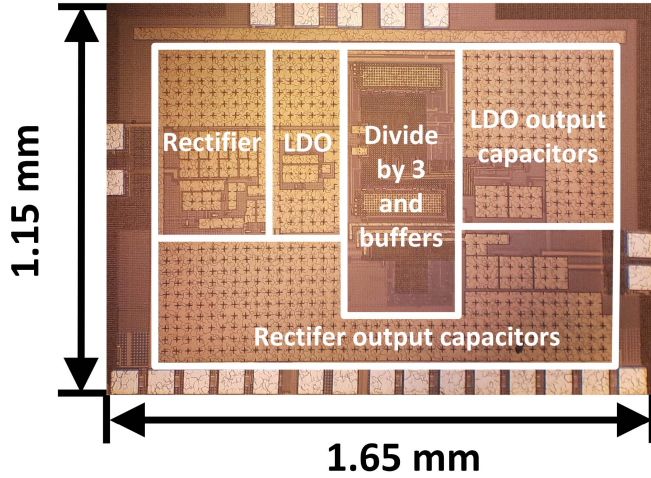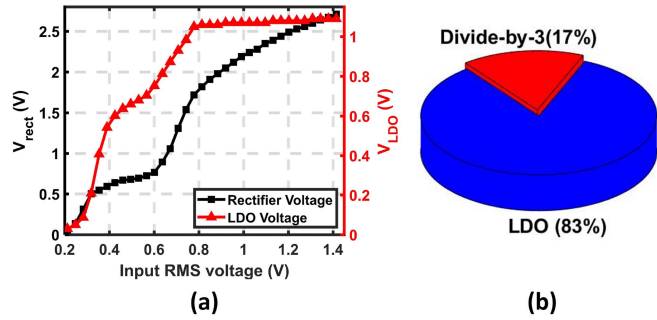
Fig. 15. Die micrograph of the IC.

Fig. 16. (a) Measured rectifier and LDO output voltages versus input rms 40.68 MHz signal (b) Breakdown of simulated power consumed by the IC. Total power consumption: 6 μW.

V. MEASUREMENT RESULTS

A. IC Functionality Verification

Fig. 15 shows the die micrograph of the IC in the proposed system. The IC has dimensions of 1.65 mm × 1.15 mm and is fabricated using TSMC 0.18 μm process. In a separate setup for wired measurements, a 40.68 MHz RF signal was connected to the input of the rectifier using an RF generator (Agilent 33250 A). The voltage at the output of the rectifier and the LDO were then measured using an oscilloscope. Fig. 16(a) shows the rectifier and LDO output voltages with respect to input RMS voltage. The rectifier output voltage increases with an increase in the input rms voltage, and the rate of increase starts to reduce after a certain input rms voltage. This is due to the reduction in PCE of the rectifier as the input power is increased. The LDO generates a stable DC voltage of 1.05 V for an input rms voltage above 0.8 V. The LDO output voltage is close to the simulated value of 1.1 V. The total simulated power consumption of the IC is equal to 6 μW. Fig. 16(b) shows the breakdown of the power consumption of the IC. The LDO dominates the power consumption of the IC.

B. Localization System Verification

Fig. 17(a) illustrates the measurement setup for verifying the proposed localization system. The objective of this measurement
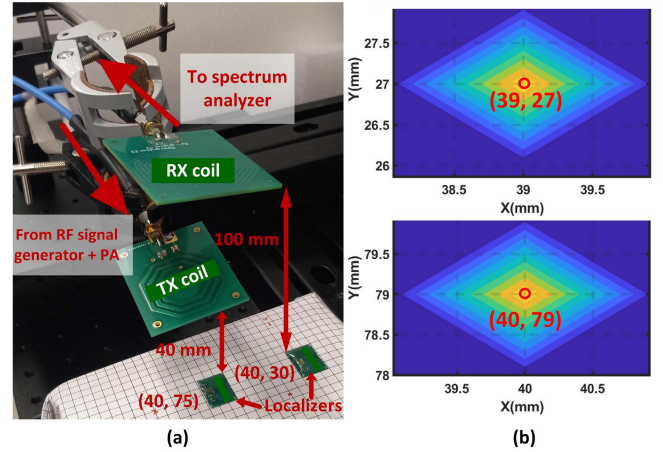

Fig. 17. (a) Measurement setup for verifying the proposed localization system (b) Obtained coordinates for the center of the localizers at (40, 30) mm (top) and (40, 75) mm (bottom).
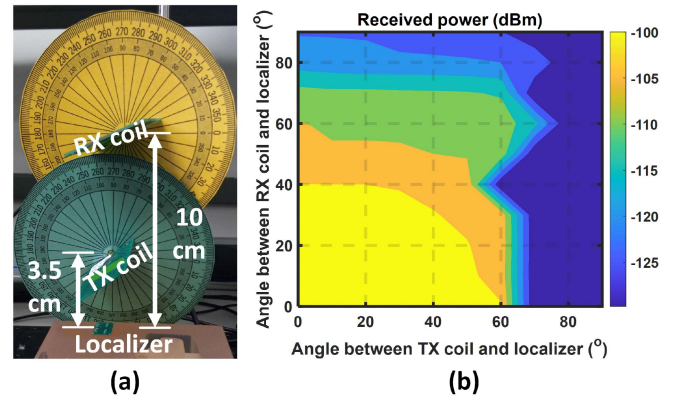

Fig. 18. (a) Measurement setup used for obtaining received power profile with respect to different angular orientations of the TX and RX coil (b) Received 13.56 MHz signal power in dBm across different angular orientations of the TX and RX coil.

was to ascertain the position of two localizers at known locations. Therefore, the localizers are placed on a surface, and one edge of the surface is fixed to be the origin. The centers of the localizers are fixed at known coordinates of (40, 30) mm and (40, 75) mm. A 40.68 MHz RF signal having −20 dBm power is generated using the RF signal generator. A power amplifier (PA) (Mini-circuits ZHL-20W-13+) was connected in cascade with the RF signal generator to increase the operating range of the wireless link. The PA has a small-signal gain of 50 dB and a saturated output power of 43 dBm. Therefore, the boosted RF signal of 30 dBm power is delivered to the TX coil for wireless powering of the IC. The TX coil is placed at a distance of 4 cm from the localizers. The localizers generate the divide-by-3 signal and transmit back the 13.56 MHz signal to the RX coil, which is placed at a distance of 10 cm from the localizers. Motorized rails (Thorlabs LTS300) are interfaced with MATLAB and used to automate the simultaneous movement of the TX and RX coils to scan the entire area with a 1 mm resolution in the X and Y directions. At each coordinate, the spectrum is recorded using a spectrum analyzer (Keysight PXA Signal Analyzer N9030 A)
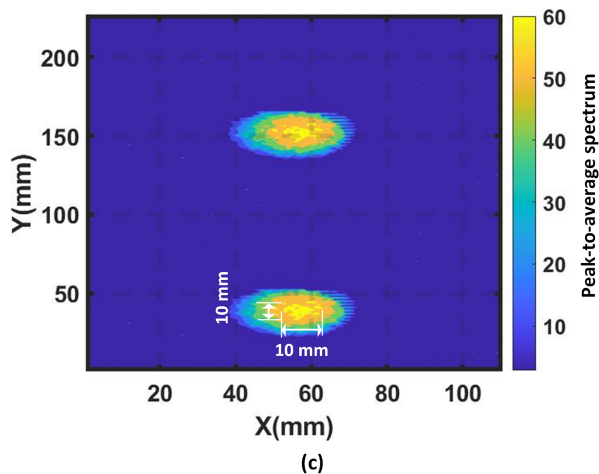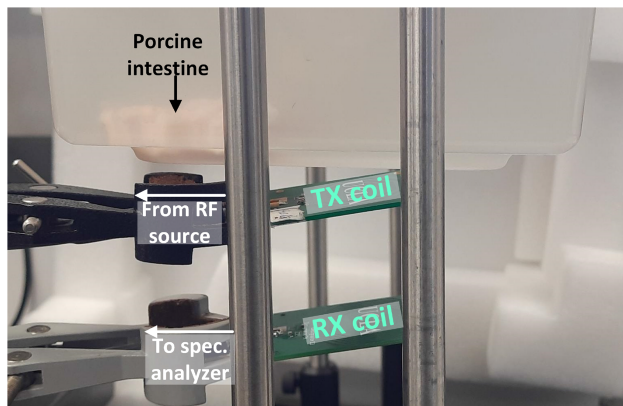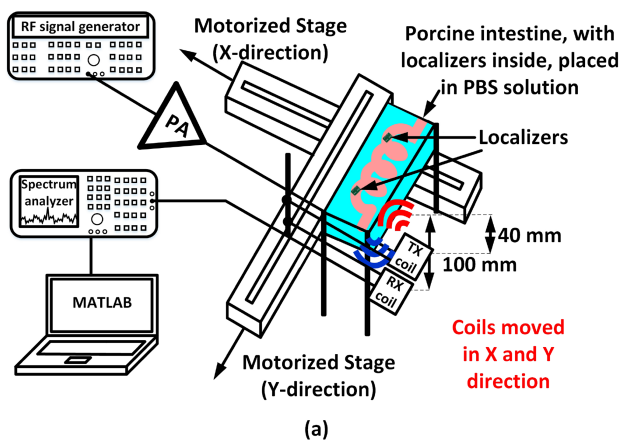
Fig. 19.   (a) Schematic and (b) picture of the setup for ex vivo verification of the proposed localization system inside porcine intestine; (c) Contour plot of the peak-to-average spectrum of the spectrum received at each coordinate. The brighter regions indicate a greater magnitude of the received 13.56 MHz signal.
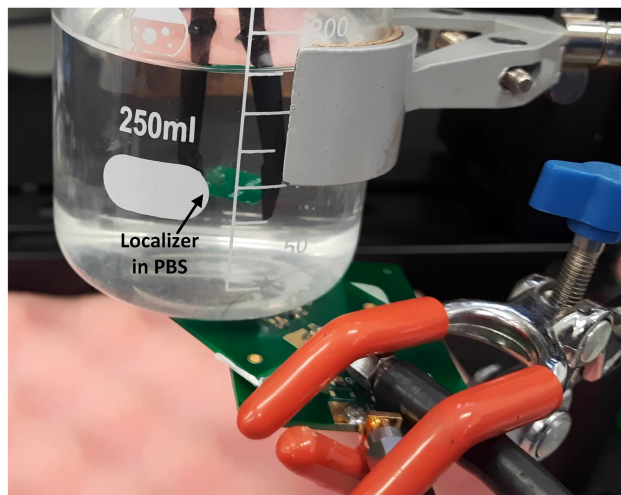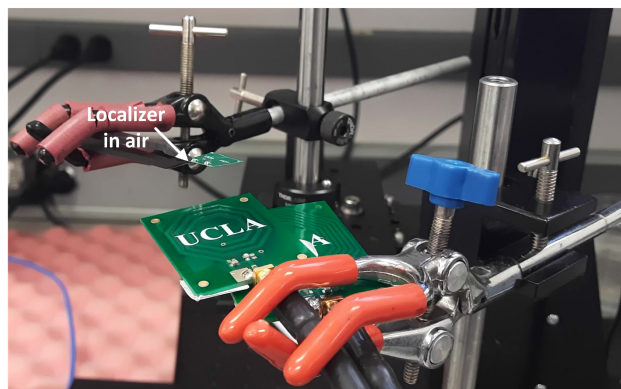

Fig. 20.   (a) Schematic of the measurement setup for sensing the rate of physiological motion; (b) picture of the setup when localizer is in air and (c) when it is in PBS solution.

connected to the RX coil. The spectrum analyzer is also interfaced with a laptop for data processing using MATLAB. The coordinate with the maximum received signal power is extracted as the experimentally obtained locations. Fig. 17(b) depicts the extracted coordinates obtained for the localizers placed at (40, 30) mm and (40, 75) mm. The obtained coordinates have an error of less than 5 mm.

Using a measurement setup described in [27] and also illustrated in Fig. 18(a), two paper protractors are added around the TX and RX coils, and the coils are then rotated to measure the received power of the 13.56 MHz signal at different angular orientations of the TX and RX coils with respect to the localizer. For the purpose of this experiment, a separation of 3.5 cm is used between the TX coil and the localizer, while a separation

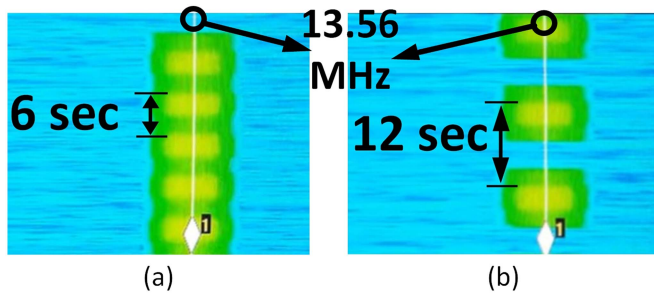Fig. 21. Spectrogram for motion rates of (a) 10 and (b) 5 beats per minute. Brighter regions indicate a stronger received 13.56 MHz tone.

of 10 cm is used between the RX coil and the localizer. The noise floor for these measurements is observed to be at −128 dBm. Fig. 18(b) illustrates the contour plot of the received power across different angular orientations. In case of misalignment between the TX/RX coil and the localizer, it can be observed that the received power (and consequently SNR) reduces, but this does not affect the spread of the received power, which is determined by the size of the localizer coils. Therefore, the misalignment does not increase localization error. If the minimum SNR required is constrained to 20 dB (chosen only for the purpose of quantifying an acceptable level of misalignment), it can be observed that the system is fairly robust to angular misalignments of up to 60° between the TX coil and localizer and up to 70° between the RX coil and localizer. Increasing (decreasing) the minimum SNR requirement leads to the detection of the 13.56 MHz tone for smaller (larger) angular misalignments between the TX/RX coil and the localizer.

A measurement setup illustrated by Fig. 19(a) is used for ex vivo verification of the localization system using porcine intestine. Two localizers are placed in an unknown location inside the porcine intestine, and the intestine is placed inside a container filled with phosphate-buffered saline (PBS) solution. This is done to mimic the characteristics of animal tissue closely. The localizer is encapsulated with a thick layer of ultraviolet (UV) light-cured epoxy resin (BONDIC) before being used for the ex vivo measurement to prevent water and/or PBS solution from leaking into the microchip and causing electrostatic discharge (ESD). A 40.68 MHz RF signal of 36 dBm power is used in this experiment for wireless powering of the IC. A higher power is required due to the extra attenuation of the RF signal as it passes through the bottom of the container, PBS solution, and the intestine. The TX and RX coils were automated to move simultaneously using motorized rails with a resolution of 1 mm in both X and Y directions to scan the bottom surface of the container. Fig. 19(b) shows a picture of the measurement setup. At each coordinate, the spectrum is recorded by the spectrum analyzer and sent to MATLAB for processing. The peak-to-average ratio of the spectrum is used to quantify the strength of the received 13.56 MHz tone with respect to the noise floor. Fig. 19(c) shows the contour plot of the entire area constructed using peak-to-average values of the received spectrum at each coordinate. Assuming the estimated location of the localizers to be within the region with the brightest contour, the maximum
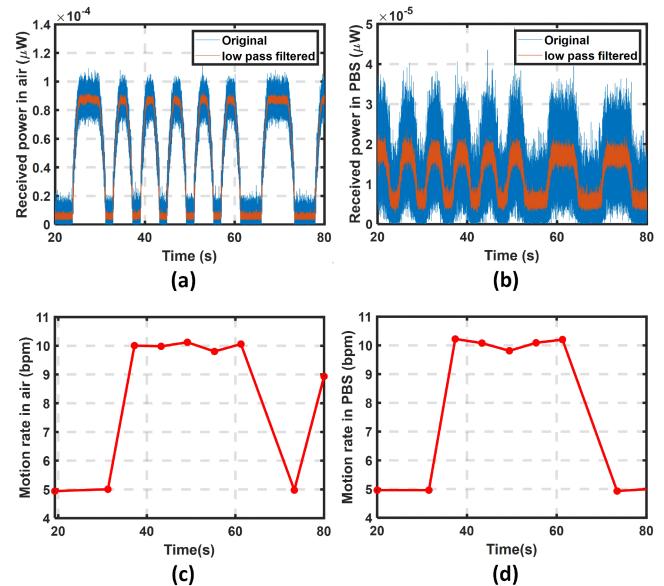

Fig. 22. Received signal power magnitude from the spectrogram when the localizer is placed in (a) air and (b) PBS solution before and after filtering; Extracted motion rates in (c) air and (d) PBS solution.
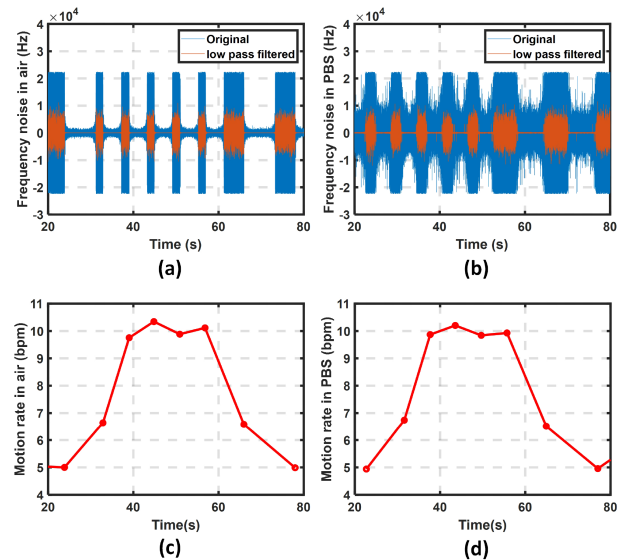

Fig. 23. Frequency noise in the received spectrogram when the localizer is placed in (a) air and (b) PBS solution before and after filtering. The frequency noise is more when the localizer is not powered; Extracted motion rates when the localizer is placed in (c) air and (d) PBS solution.

possible localization error in both dimensions for the raw data is ±5 mm. The error depends on the spatial region where there is sufficient coupling between the TX/RX coil and the localizer coil. Since the localizer coils are much smaller than the TX/RX coils, the detection error is strongly related to the physical size of the localizer coils (which have a radius of 4 mm). It is important to note that the maximum error, in this case, is limited by the diameter of the localizer coil. Therefore, a smaller error could be obtained if a smaller localizer coil is used to transmit back. However, a smaller coil might lead to a reduction in the operating range of the system.
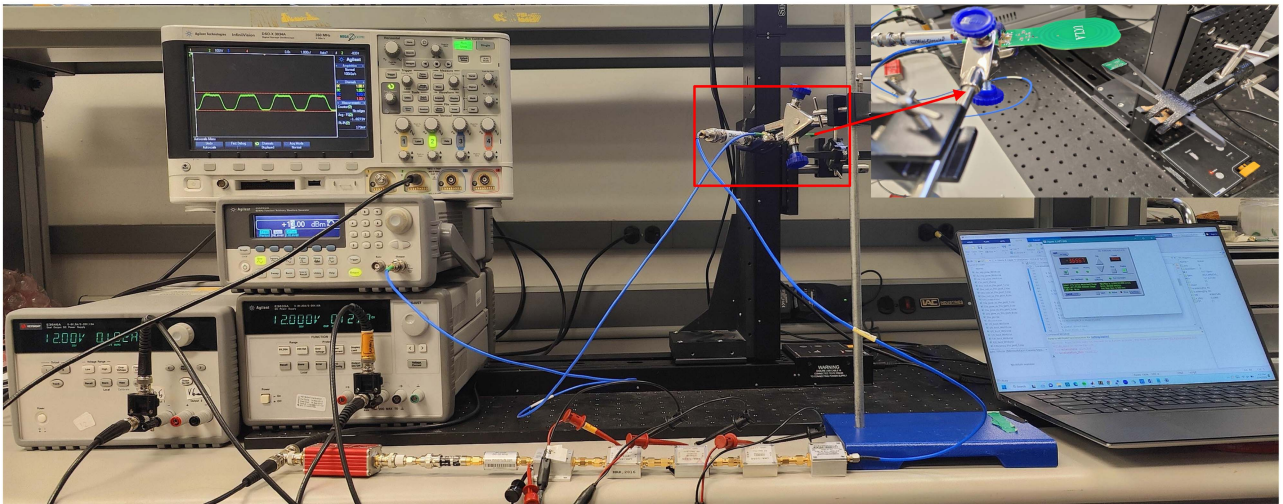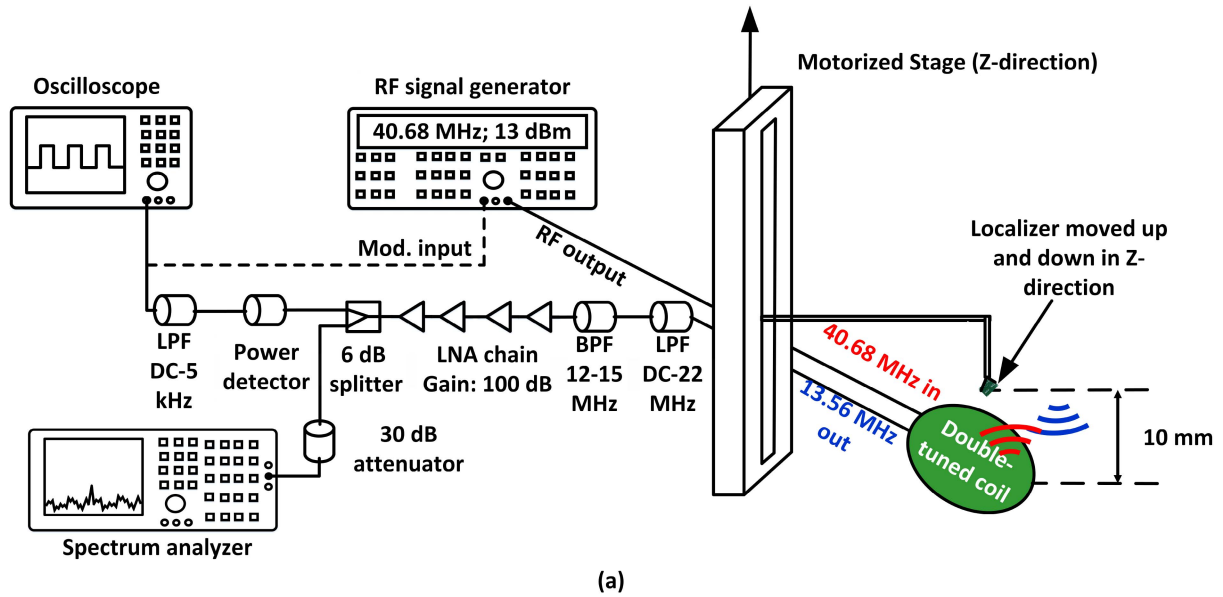
Fig. 24. (a) Schematic and (b) picture of the measurement setup for sensing the distance moved by the localizer.

C. Physiological Motion Sensing

1) Sensing the Rate of Motion: The functionality of sensing the rate of physiological motion is verified using the measurement setup as shown in Fig. 20(a). In two different variations of the measurement, the localizer is placed in (i) air and (ii) PBS solution and periodically moved up and down by 4 mm at rates of (a) 10 and (b) 5 beats per minute using a motorized rail (Thorlabs LTS300). Fig. 20(b) shows the picture of the setup when the localizer is placed in air, while (c) shows the picture when the localizer is placed in PBS solution. Similar to the previous experiment, a 40.68 MHz RF signal of 36 dBm power is delivered to the TX coil for wireless powering. The TX and RX coils are kept in a fixed position during this measurement, at average distances of 4 cm and 10 cm, respectively, from the localizer. The spectrum analyzer, connected to the RX coil, records the variation of the received spectrum around 13.56 MHz

with time for the entire duration of this measurement. Fig. 21(a) and (b) show the received spectrogram for the motion rates of 10 and 5 beats per minute, respectively. For the measurements in both air and PBS, the magnitude and phase information of the spectrogram is then lowpass filtered to remove the 60 Hz supply noise, and the motion rate is extracted using MATLAB.

Fig. 22(a) and (b) depict the signal power magnitude obtained from the magnitude of the received spectrogram when the localizer is placed in air and PBS solution, respectively. It can be observed that the received signal power is around 90 pW when the coils are closest to the localizer and drops to almost zero when the coils are farthest. Fig. 22(c) and (d) depict the extracted motion rates from the received signal power when the localizer is placed in air and PBS solution, respectively. Fig. 23(a) and (b) depict the frequency noise obtained from the phase of the received spectrogram when the localizer is placed in air and PBS solution, respectively. The frequency noise is

TABLE III
PERFORMANCE COMPARISON WITH PREVIOUS LOCALIZATION SYSTEMS

	This work	Nature Elec. '23 [18]	SSC-L '23 [17]	JSSC '18 [16]	Nature Bio. '17 [15]
Technology (μm)	0.18	N/A*	0.18	0.18	0.18
Wireless power**	Yes	No	No	No	No
Downlink frequency (MHz)	40.68	2400	2.048	40	500
Uplink frequency (MHz)	13.56	2400	57	160	480-520
Avg. power (μW)	6	180-240	336	9880	339
Excitation power (W)	2	60	NM****	N/A*	NM****
Excitation coil size (number)	3.5 cm diameter (1)	X and Y coils: 60 cm × 30 cm Z coil: 60 cm diameter (1)	10 cm × 10 cm (6)	N/A*	0.5 cm diameter (1)
Localization dimension	2D	3D	3D	2D	2D
Localization modality	RF with inductive magnetic coupling	Magnetic gradient; spatial encoding	Inductive magnetic field	RF	Magnetic gradient; frequency encoding
Accuracy (mm)	< 5***	<7.5	<1	<10	<1
Measurement latency (ms)	11.3	300	1000	<NM****	5
Motion detection	Yes	No	No	No	No
Point-of-care application	Yes	Yes	No	Yes	Yes

*N/A: Not Applicable   **No wireless data transfer   ***Raw data; no data processing   ****NM: Not mentioned

defined as the difference between the expected signal frequency (13.56 MHz) and the frequency of the maximum tone received. It can be observed that the frequency noise is much larger when the coils are farthest from the localizer because the localizers are not powered in this position, and the received signal almost entirely consists of noise. The frequency noise is much lesser when the coils are closest to the localizer. Fig. 23(c) and (d) depict the extracted motion rates from the frequency noise of the received signal when the localizer is placed in air and PBS solution, respectively.

2) Sensing the Distance Moved: Another measurement setup, as illustrated by Fig. 24(a), is used to sense the distance moved by the localizer. Fig. 24(b) shows the picture of the setup. The power of the received signal is also used to modulate the 40.68 MHz TX power signal, causing savings in TX power. This improves the link efficiency for wireless powering while maintaining a minimum SNR for the received signal. For this measurement, a double-tuned double-input coil, the details of which are given in [28], is used. The double-tuned coil is matched to the frequencies of 40.68 MHz (HF) and 13.56 MHz (LF) at the HF and LF inputs, respectively. It has a matching of -26.2 dB and -21.5 dB at HF and LF, respectively, and an isolation of -17.7 dB and -11.7 dB at each port. This coil acts as both the TX and RX coil and has been shown to reduce inter-coil couplings compared to a two-coil system (separate TX and RX coils). The localizer is placed at a distance of 10 mm from the double-tuned coil and is periodically moved up and down in the Z-direction by distances ranging from 50 to 1000 μm using a motorized rail (Thorlabs LTS300). A 40.68 MHz RF signal of 13 dBm power is delivered to the double-tuned coil for wireless powering. Although a larger operating range can be obtained using a higher TX power, it significantly increases the coupling of the 40.68 MHz signal to the output, requiring more aggressive filtering to reject this coupled signal. It is important to note that the cascade of filters to reject the coupled 40.68 MHz signal is optional and has been used only to ensure that the received

13.56 MHz signal is visible in the time domain using an oscilloscope. The motion detection measurements can be performed using just the spectrum analyzer to record a spectrogram of the received signal in the time domain.

Since the power of the received 13.56 MHz signal at the LF input is needed to generate the modulation input for the 40.68 MHz RF source, it is filtered out, and the 40.68 MHz coupled signal is rejected using the cascade of a low-pass filter (LPF) having a cut-off frequency of 22 MHz (Mini-Circuits BLP-21.4+) and a band-pass filter (BPF) having a passband between 12 and 15 MHz (Mini-Circuits ZFBP-13.5S+). The signal obtained after filtering is passed through a chain of low-noise amplifiers (RF Bay LNA-1050, RF Bay LNA-1800, and RF Bay LNA-500H), providing a total gain of 100 dB. The resultant signal is then passed through a 6 dB splitter (Mini-Circuits ZFRSC-42-S+), and one of the branches is connected to a 30 dB attenuator followed by the spectrum analyzer (Keysight PXA N9030 A). The other branch is used for detecting the power of the amplified and filtered signal using a power detector (HP 8473 C). The power detector output is passed through an LPF with a cut-off frequency of 5 kHz (Thorlabs EF114) and sent to the oscilloscope for sensing. Fig. 25 shows the spectrum of the signal at the input of the power detector, while Fig. 26(a), (b), (c), (d), and (e) shows the oscilloscope waveforms obtained when the localizers are moved by a distance of 50, 100, 200, 500 and 1000 μm respectively. Fig. 26(f) shows the peak-to-peak voltage obtained at the oscilloscope with respect to the distance moved.

The oscilloscope input is then also connected to the modulation input of the RF signal source that generates the 40.68 MHz TX signal. When the localizer is closer to the double-tuned coil, an increase in the power detected leads to a more negative DC voltage generated at its output. When this voltage is fed back to the RF source, it reduces the power of the 40.68 MHz TX signal. Similarly, when the localizer is farther away, a decrease in the power detected increases the power of the 40.68 MHz TX signal. Therefore, this leads to savings in TX power. The modulation
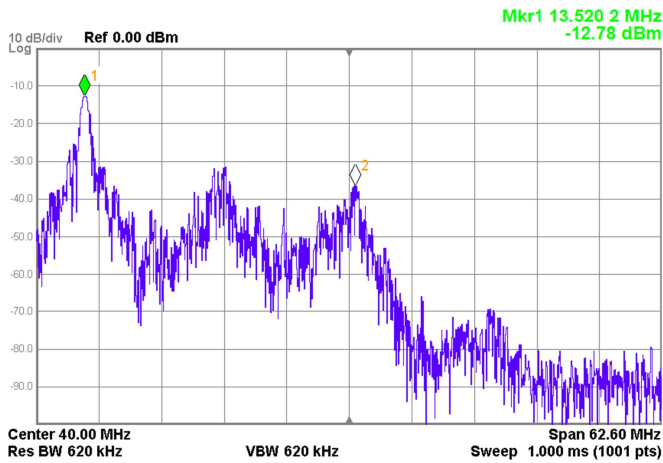
Fig. 25. Spectrum of the signal at the input of the power detector after it is attenuated by 30 dB. Isolation of more than -20 dB is achieved between the received 13.56 MHz tone and the coupled 40.68 MHz tone.
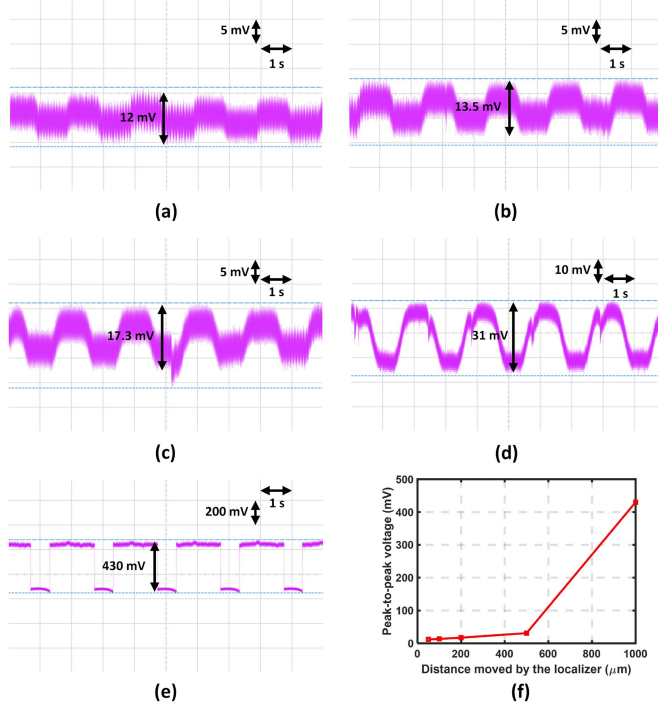

Fig. 26. Oscilloscope waveforms obtained when the localizer moves by (a) 50 (b) 100 (c) 200 (d) 500 and (e) 1000 μm (f) Peak-to-peak voltage versus distance moved by the localizer.

index of the RF signal source determines the savings in TX power. At a modulation index of 100%, the TX power can be reduced by a maximum of 3 dB. Fig. 27(a), (b), and (c) shows the oscilloscope waveforms obtained when the oscilloscope input is connected to the modulation input of the RF source, and the localizers are moved by a distance of 200, 500, and 1000 μm respectively. Fig. 27(d) shows the peak-to-peak voltage obtained at the oscilloscope with respect to the distance moved.

Table III compares the performance of this system with previous localization systems.
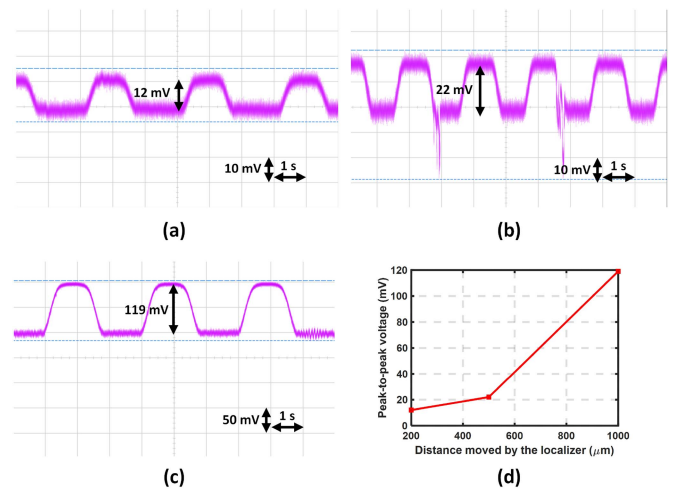

Fig. 27. Oscilloscope waveforms obtained when the oscilloscope input is connected to the modulation input of the RF source, and the localizer moves by (a) 200 (b) 500 and (c) 1000 μm (d) Peak-to-peak voltage versus distance moved by the localizer in this case.

VI. CONCLUSION

A fully battery-less wirelessly powered localization system with an ultra-low average power consumption of 6 μW has been presented here. The low power consumption of the IC, fabricated in 0.18 μm technology, is due to the sub-harmonic locking scheme, which uses the RF power signal to generate the signal transmitted by the localizer. This enables it to be reliably powered wirelessly at a distance of 40 mm with a minimum TX power of 2 W. The localization system has an error of less than 5 mm, and this has been verified ex vivo using a porcine intestine. Moreover, it has also been verified to detect a motion as small as 50 μm, as well as rates of motion up to 10 beats per minute. The received signal for this system has also been used to control the power of the transmitter adaptively, leading to further savings in the TX power of the system. Due to its extremely small form factor of 17 mm $\times$ 12 mm $\times$ 0.2 mm, the localizer can be fabricated on a flexible polyimide substrate, enabling it to be used inside 000-sized capsules for next-generation WCE and other biomedical sensor network applications.

REFERENCES

[1] S. M. R. Islam, D. Kwak, M. H. Kabir, M. Hossain, and K. -S. Kwak, "The Internet of Things for health care: A comprehensive survey," *IEEE Access*, vol. 3, pp. 678–708, 2015.

[2] S. Amendola, R. Lodato, S. Manzari, C. Occhiuzzi, and G. Marrocco, "RFID technology for IoT-based personal healthcare in smart spaces," *IEEE Internet Things J.*, vol. 1, no. 2, pp. 144–152, Apr. 2014, doi: 10.1109/JIOT.2014.2313981.

[3] X. Jia, Q. Feng, T. Fan, and Q. Lei, "RFID technology and its applications in Internet of Things (IoT)," in *Proc. IEEE 2nd Int. Conf. Consum. Electron. Commun. Netw.*, 2012, pp. 1282–1285, doi: 10.1109/CEC-Net.2012.6201508.

[4] D. Puccinelli and M. Haenggi, "Wireless sensor networks: Applications and challenges of ubiquitous sensing," *IEEE Circuits Syst. Mag.*, vol. 5, no. 3, pp. 19–31, May 2005, doi: 10.1109/MCAS.2005.1507522.

[5] D. Kandris, C. Nakas, D. Vomvas, and G. Koulouras, "Applications of wireless sensor networks: An up-to-date survey," *Appl. Syst. Innov.*, vol. 3, no. 1, pp. 1–24, 2020.

[6] D. Sarikaya, J. J. Corso, and K. A. Guru, "Detection and localization of robotic tools in robot-assisted surgery videos using deep neural networks for region proposal and detection," *IEEE Trans. Med. Imag.*, vol. 36, no. 7, pp. 1542–1549, Jul. 2017, doi: 10.1109/TMI.2017.2665671.

[7] I. Vlachos, B. Krishnan, D. M. Treiman, K. Tsakalis, D. Kugiumtzis, and L. D. Iasemidis, "The concept of effective inflow: Application to interictal localization of the epileptogenic focus from iEEG," *IEEE Trans. Biomed. Eng.*, vol. 64, no. 9, pp. 2241–2252, Sep. 2017, doi: 10.1109/TBME.2016.2633200.

[8] R. Jin and B. Jung, "Magnetic tracking system for heart surgery," *IEEE Trans. Biomed. Circuits Syst.*, vol. 16, no. 2, pp. 275–286, Apr. 2022, doi: 0.1109/TBCAS.2022.3163172.

[9] T. D. Than, G. Alici, H. Zhou, and W. Li, "A review of localization systems for robotic endoscopic capsules," *IEEE Trans. Biomed. Eng.*, vol. 59, no. 9, pp. 2387–2399, Sep. 2012, doi: 10.1109/TBME.2012.2201715.

[10] H. Mateen, R. Basar, A. U. Ahmed, and M. Y. Ahmad, "Localization of wireless capsule endoscope: A systematic review," *IEEE Sensors J.*, vol. 17, no. 5, pp. 1197–1206, Mar. 2017, doi: 10.1109/JSEN.2016.2645945.

[11] G. L. Barbruni, P. M. Ros, D. Demarchi, S. Carrara, and D. Ghezzi, "Miniaturised wireless power transfer systems for neurostimulation: A review," *IEEE Trans. Biomed. Circuits Syst.*, vol. 14, no. 6, pp. 1160–1178, Dec. 2020, doi: 10.1109/TBCAS.2020.3038599.

[12] A. Costanzo and D. Masotti, "Energizing 5G: Near- and far-field wireless energy and data transfer as an enabling technology for the 5G IoT," *IEEE Microw. Mag.*, vol. 18, no. 3, pp. 125–136, May 2017, doi: 10.1109/MMM.2017.2664001.

[13] B. Razavi, "The role of PLLs in future wireline transmitters," *IEEE Trans. Circuits Syst. I: Regular Papers*, vol. 56, no. 8, pp. 1786–1793, Aug. 2009.

[14] Y. Sun and A. Babakhani, "A wirelessly powered injection-locked oscillator with on-chip antennas in 180-nm SOI CMOS for spectroscopy application," *IEEE Sensors Lett.*, vol. 3, no. 7, Jul. 2019, Art. no. 5500704.

[15] B. Jamali and A. Babakhani, "Wireless time transfer with subpicosecond accuracy based on a fully integrated injection-locked picosecond pulse detector," *IEEE Trans. Microw. Theory Techn.*, vol. 68, no. 1, pp. 160–169, Jan. 2020.

[16] H. Rahmani, Y. Sun, M. Kherwa, S. Pal, and A. Babakhani, "Coherent radiation from a swarm of wirelessly powered and synchronized sensor nodes," *IEEE Sensors J.*, vol. 20, no. 19, pp. 11608–11616, Oct. 2020, doi: 0.1109/JSEN.2020.2996571.

[17] M. Monge, A. Lee-Gosselin, M. G. Shapiro, and A. Emami, "Localization of microscale devices in vivo using addressable transmitters operated as magnetic spins," *Nature Biomed. Eng.*, vol. 1, no. 9, pp. 736–744, Sep. 2017, doi: https://doi.org/10.1038/s41551-017-0129-2.

[18] M. Rustom and C. Sideris, "Design and implementation of a low power wireless frequency-division multiplexed magnetic 3D localization scheme with sub-mm precision for capsule endoscopy applications," *IEEE Solid-State Circuits Lett.*, vol. 6, pp. 37–40, 2023, doi: 10.1109/LSSC.2023.3238351.

[19] J. Jang et al., "A four-camera VGA-resolution capsule endoscope system with 80-Mb/s body channel communication transceiver and sub-centimeter range capsule localization," *IEEE J. Solid-State Circuits*, vol. 54, no. 2, pp. 538–549, Feb. 2019, doi: 10.1109/JSSC.2018.2873630.

[20] S. Sharma et al., "Location-aware ingestible microdevices for wireless monitoring of gastrointestinal dynamics," *Nature Electron.*, vol. 6, pp. 1–15, Feb. 2023.

[21] A. Ray, I. Habibagahi, and A. Babakhani, "Fully wireless and batteryless localization and physiological motion detection system for point-of-care biomedical applications," in *Proc. IEEE Biomed. Circuits Syst. Conf.*, 2022, pp. 26–30, doi: 10.1109/BioCAS54905.2022.9948647.

[22] P. Pérez-Nicoli, F. Silveira, and M. Ghovanloo, *Inductive Links for Wireless Power Transfer*. Berlin, Germany: Springer, 2021.

[23] I. Habibagahi et al., "Vagus nerve stimulation using a miniaturized wirelessly powered stimulator in pigs," *Sci. Rep.* vol. 12, 2022, Art. no. 8184.

[24] J. Jang, I. Habibagahi, H. Rahmani, and A. Babakhani, "Wirelessly powered, batteryless closed-loop biopotential recording IC for implantable leadless cardiac monitoring applications," in *Proc. IEEE Biomed. Circuits Syst. Conf.*, 2021, pp. 1–4, doi: 10.1109/BioCAS49922.2021.9644988.

[25] U. Guler and M. Ghovanloo, "Power management in wireless power-sipping devices: A survey," *IEEE Circuits Syst. Mag.*, vol. 17, no. 4, pp. 64–82, Fourthquarter 2017, doi: 10.1109/MCAS.2017.2757090.

[26] B. Razavi, "The low dropout regulator [a circuit for all seasons]," *IEEE Solid-State Circuits Mag.*, vol. 11, no. 2, pp. 8–13, Spring 2019, doi: 10.1109/MSSC.2019.2910952.

[27] A. Ray and A. Babakhani, "A wirelessly powered system of coherent sensing nodes for fracture mapping applications at temperatures upto 250°C and pressures upto 24MPa," *IEEE Sensors J.*, vol. 23, no. 10, pp. 10605–10615, May 2023, doi: 10.1109/JSEN.2023.3263051.

[28] I. Habibagahi, R. P. Mathews, A. Ray, and A. Babakhani, "Design and implementation of multisite stimulation system using a double-tuned transmitter coil and miniaturized implants," *IEEE Microw. Wireless Technol. Lett.*, vol. 33, no. 3, pp. 351–354, Mar. 2023, doi: 10.1109/LMWC.2022.3217519.

Arkaprova Ray (Graduate Student Member, IEEE) received the B.Tech. and M.Tech. degrees in electronics and electrical communication engineering with a specialization in microelectronics and VLSI design from the Indian Institute of Technology Kharagpur, Kharagpur, India, in 2020. He is currently working toward the Ph.D. degree in electrical and computer engineering with the University of California at Los Angeles, Los Angeles, CA, USA, under the supervision of Prof. Aydin Babakhani. His research interests include design and implementation of miniaturized wirelessly powered sensors for different biomedical and industrial applications

Iman Habibagahi (Graduate Student Member, IEEE) received the B.Sc. degree in electrical engineering from the Sharif University of Technology, Tehran, Iran, in 2019, and the M.Sc. degree from the University of California at Los Angeles (UCLA), Los Angeles, CA, USA, in 2021. He is currently working toward the Ph.D. degree from UCLA advised by Prof. A. Babakhani. His research interests include low-power integrated circuit design, wireless power harvesting, and wireless technologies for biomedical implants. Mr. Habibagahi received the UCLA ECE Department Fellowship. He was also the recipient of the radio frequency integrated circuit (RFIC)'22 NSF Student Travel Award.

Aydin Babakhani (Senior Member, IEEE) received the B.S. degree in electrical engineering from the Sharif University of Technology, Tehran, Iran, in 2003 and the M.S. and Ph.D. degrees in electrical engineering from Caltech, Pasadena, CA, USA, in 2005 and 2008, respectively. He was an Associate Professor with the Electrical and Computer Engineering Department, Rice University, Houston, TX, USA, and also the Director of the Rice Integrated Systems and Circuits Laboratory. He was a Postdoctoral Scholar with Caltech in 2009 and a Research Scientist with the IBM Thomas J. Watson Research Center, New York, NY, USA, in 2010. He was a Louis Owen Junior Chair Assistant Professor from 2016 to 2017 and an Assistant Professor of ECE from 2011 to 2016 with Rice University. He is currently an Associate Professor with the Electrical and Computer Engineering Department, University of California at Los Angeles (UCLA), Los Angeles, CA, USA, and also the Director of UCLA Integrated Sensors Laboratory. He is also a Member of DARPA Microsystems Exploratory Council and co-founded MicroSilicon, Inc., and Maxwell Biomedical, Inc. He has authored or coauthored more than 85 articles in peer-reviewed journals and conference proceedings and 21 issued or pending patents. His research is supported by NSF, DARPA, AFOSR, ONR, the W. M. Keck Foundation, SRC, and more than 10 companies. He was the recipient of the multiple best paper awards, including the Best Paper Award at IEEE SiRF Conference in 2016, Best Paper Award at IEEE RWS Symposium in 2015, Best Paper Award at IEEE IMS Symposium in 2014, and the 2nd-place in Best Paper Awards at IEEE APS Symposium 2016 and IEEE IMS Symposium 2016, Bell Labs Prize in 2018, prestigious NSF CAREER Award in 2015, Innovation Award from Northrop Grumman in 2014, and DARPA Young Faculty Award in 2012, and Caltech Electrical Engineering Department's Charles Wilts Best Ph.D. Thesis Prize for his work titled Near-Field Direct Antenna Modulation. He was also the recipient of the Microwave Graduate Fellowship in 2007, Grand Prize in the Stanford- Berkeley-Caltech Innovators Challenge in 2006, Analog Devices, Inc., Outstanding Student Designer Award in 2005, and Caltech Special Institute Fellowship, and Atwood Fellowship in 2003. He was also the Gold Medal winner at both the National Physics Competition in 1998 and the 30th International Physics Olympiad in Padova, Italy, in 1999.